# Spatial analysis reveals distinct immune phenotypes and tertiary lymphoid structure-like aggregates in pediatric acute myeloid leukemia

Joost B. Koedijk[1,2], Inge van der Werf[1,3], Marijn A. Vermeulen[1], Alicia Perzolli[1,2], Marta Fiocco[1,4,5], Hester A. de Groot-Kruseman[1], Rubina Moeniralam[1], Stefan Nierkens[1,6], Mirjam E. Belderbos[1], C. Michel Zwaan[1,2#], Olaf Heidenreich[1,7#*]

[1]Princess Máxima Center for Pediatric Oncology, 3584 CS Utrecht, The Netherlands.

[2]Department of Pediatric Oncology, Erasmus MC/Sophia Children's Hospital, 3015 GD Rotterdam, The Netherlands.

[3]Oncode Institute, 3521 AL, Utrecht, The Netherlands

[4]Mathematical Institute, Leiden University, Leiden, The Netherlands

[5]Department of Biomedical Data Sciences, Leiden University Medical Center, Leiden, The Netherlands.

[6]Center for Translational Immunology, University Medical Center Utrecht, 3584 CX Utrecht, The Netherlands.

[7]Wolfson Childhood Cancer Research Centre, Newcastle University, Newcastle upon Tyne NE1 7RU, UK.

[#]Equal contribution

*Corresponding author: Olaf Heidenreich, Princess Máxima Center for Pediatric Oncology, 3584 CS Utrecht, The Netherlands. Phone: 088-9727272; E-mail: o.t.heidenreich@prinsesmaximacentrum.nl

**Running title:** The spatial immune landscape of pediatric AML

**Disclosure of conflicts of interest:** The authors declare no financial conflicts of interest.

**Figures/Tables:** 5 Main Figures, 3 Supplementary Figures, 3 Supplementary Tables.

**Words (excl. references):** 4858 **References:** 50

**Keywords:** spatial transcriptomics, bone biopsy, secondary lymphoid organs, ectopic T cell networks, hematological malignancies.

**Abstract**

Pediatric cancers are characterized by a relatively low mutational burden and therefore, children are thought to be poor candidates for T cell-engaging immunotherapies. Here, we performed a multidimensional characterization of the tumor immune microenvironment in newly diagnosed children with acute myeloid leukemia (AML) and non-leukemic controls. We identified a subset of pediatric AML patients with remarkably high levels of T cell infiltration and a relatively low abundance of anti-inflammatory macrophages in the bone marrow. In addition, we detected large T cell networks that colocalized with B cells in immune-infiltrated samples, resembling tertiary lymphoid structures as described in solid tumors. Using spatial transcriptomics, we dissected the composition of these structures and revealed unique hotspots of anti-tumor immunity. This work raises the possibility that a subset of pediatric AML patients may benefit from T cell-engaging immunotherapies and encourages further study of these lymphoid structures in the context of immunotherapy in AML.

**Statement of significance:** A subset of pediatric AML patients harbors hotspots of anti-tumor immunity in the tumor microenvironment. The presence of tertiary lymphoid structure-like aggregates in the bone marrow of pediatric AML encourages the evaluation of T cell-engaging immunotherapies in this population, as well as the development of novel antibody-based and cellular therapies.

A tumor microenvironment that is infiltrated by cytotoxic T cells is of crucial importance to elicit a response to T cell-engaging immunotherapies such as immune checkpoint inhibitors and bispecific antibodies[1]. In contrast, patients with an immune-depleted or 'cold' tumor microenvironment show significantly reduced response rates. Due to the relatively low mutational burden and the associated poor immunogenicity of pediatric cancers, children are thought to be poor candidates for T cell-engaging immunotherapies[2-3]. Among pediatric cancers, pediatric acute myeloid leukemia (AML) is a cancer with a particularly low mutational burden[4]. Nonetheless, recent evidence suggests that considerable variation in immune cell infiltration exists among cancers that are considered to be immunologically 'cold'[4-5]. For instance, in adult AML, which has a relatively low mutational burden in comparison to other adult cancer types, *TP53* mutations have been linked to relatively high immune cell infiltration in the bone marrow (BM) and improved responses to immunotherapy in comparison to *TP53*-WT adult AML[4,6-7]. However, little is known about the immune compartment in the BM of pediatric AML patients and clinical trials that evaluate the efficacy of such therapies have only recently been initiated for this population[8]. Therefore, it is unclear whether children with AML may be successfully treated with T cell-engaging immunotherapies. This prompted us to perform a multidimensional characterization of the tumor immune microenvironment in newly diagnosed children with *de novo* AML and non-leukemic controls. We identify a subset of patients with remarkably high T cell infiltration in the BM, dissect the spatial immune organization and specifically, unravel the composition of tertiary lymphoid structure-like aggregates in the BM of AML, with implications for future immunotherapy approaches.

## Results

### A subset of pediatric AML patients has remarkably high T cell infiltration in the bone marrow

For this study, we obtained 53 formalin-fixed and paraffin-embedded (FFPE) bone biopsies from a representative cohort of pediatric patients with treatment-naïve *de novo* AML (n=43), and from age- and sex-matched pediatric patients with treatment-naïve early-stage rhabdomyosarcoma without evidence of malignancy infiltrating the BM (non-leukemic controls, n=10; **Fig. 1A**). Patient characteristics are depicted in **Table S1**. Using immunohistochemistry (IHC), we found a decreased abundance of both the overall number of T cells and cytotoxic T cells in pediatric AML patients in comparison to non-leukemic controls (representative images are shown in **Fig. 1B-C**; two-sided $P = 0.006$ and $P = 0.003$, respectively; **Fig. 1D-E**). However, the extent of overall T cell and cytotoxic T cell infiltration could differ up to 90-fold between individual AML patients, with several patients showing relatively high T cell infiltration in the BM**.** Because it has previously been shown that cancer cells' genetic alterations may shape

the tumor immune microenvironment, we assessed if certain AML-associated genetic alterations were linked to the level of T cell infiltration[9]. Interestingly, most of the patients with relatively high T cell infiltration in the BM had *KMT2A*-rearranged AML, the most common cytogenetic abnormality in pediatric AML, although there was wide variation among this cytogenetic subgroup[10]. In contrast, most other cytogenetic groups showed low levels of both populations with little variation between patients, although several outliers were seen in these groups as well (**Fig 1F-G**). Collectively, we identified substantial variation in T cell infiltration in the BM of pediatric AML with a subset of patients showing a remarkably high T cell frequency in the BM.

**Immune-infiltrated leukemias are characterized by tumor-specific T cell responses and a relatively low abundance of anti-inflammatory macrophages**

To further study pediatric AML patients with a relatively high T cell abundance in the BM, we dichotomized patients into immune-infiltrated (n=8) and immune-depleted (n=35) groups using the non-leukemic controls' median value of cytotoxic T cells as the cut-off value. Subsequently, we performed immune-related gene expression profiling on a cytogenetically representative subset of immune-infiltrated (n=5) and immune-depleted (n=18) samples. Among this subset, four out of five (80%) immune-infiltrated samples had a KMT2A-rearrangement, while five out of eighteen (28%) samples in the immune-depleted group had this cytogenetic abnormality (**Table S1**). First, we focused on cytotoxicity-related- and immune checkpoint genes since their expression may give insight into the likelihood of response to immune checkpoint inhibitors. In our cohort, immune-infiltrated patients showed upregulation of both cytotoxic T cell genes (*CD8A*, *CD8B*) and cytotoxicity-related genes including *GZMK*, suggestive of enrichment of GZMK$^+$ cytotoxic T cells, which has been associated with response to PD-1 blockade in adult AML patients (**Fig. 2A**)[11]. Moreover, pediatric AML patients with an immune-infiltrated BM highly expressed *TNFRSF9* (encoding CD137) and the immune checkpoint genes *PDCD1* (encoding PD-1), *CTLA4*, *TIGIT* and *LAG3,* indicative of tumor-specific T cell responses that may be successfully reinvigorated by immune checkpoint inhibitors (**Fig. 2A**)[12-13]. Importantly, using a publicly available pediatric AML scRNAseq dataset, we confirmed that the above-mentioned checkpoint genes are mainly expressed by cytotoxic T cells, and that *TIGIT* and *LAG3* were the most widely expressed among this population (n=8 patients; **Fig. S1A-E**)[14]. Taken together, these results suggest that pediatric AML patients with an immune-infiltrated BM may show increased responses to immune checkpoint inhibitors in comparison to patients with an immune-depleted BM, and that the immune checkpoints TIGIT and LAG-3 may prove suitable targets to enhance cytotoxic T cell function in pediatric AML.

We next investigated whether we could identify differences in factors that either promote or restrict T cell infiltration in the BM. As anticipated, immune-infiltrated samples had significantly higher expression of genes related to T cell-attracting chemokines (*CXCL9*, *CXCL10*), and their corresponding receptor (*CXCR3*; **Fig. 2A**). In line with this, pathway analysis using GO biological processes indicated that immune-infiltrated samples were enriched in T cell migratory and -chemotaxis pathways, suggesting that immune-depleted samples are devoid of signals that attract T cells to the BM (**Fig. 2B**). From solid cancers, we know that macrophages in the tumor microenvironment are the main regulators of the extent of T cell infiltration into the tumor[15]. Specifically, pro-inflammatory, M1-like macrophages are known to be the primary source of T cell-attracting chemokines, while anti-inflammatory, M2-like macrophages restrict T cell infiltration into the tumor[16]. Previously, a specific M2-like macrophage signature has been generated for five cancer types including AML and therefore, we investigated the abundance of M2-like macrophages in our pediatric AML cohort[17]. Interestingly, the estimated abundance of M2-like macrophages was inversely correlated with both the total T cell and cytotoxic T cell frequency in the BM (Spearman's $r$ = -0.76 [95% CI: -0.89 to -0.51], $P < 0.001$, $r$ = -0.64 [95% CI: -0.83 to -0.30], $P = 0.001$, respectively; **Fig. 2C** and **Fig. S1F**). Concordantly, we identified a significantly decreased M2-like macrophage abundance in immune-infiltrated samples compared to immune-depleted samples (two-sided $P < 0.001$; **Fig. 2D**). Notably, immune-depleted samples had significantly higher expression of the gene encoding arginase type II (*ARG2*), which is known to be crucial for AML blast-mediated polarization of monocytes into an M2-like phenotype[18]. Next, because it is unknown whether the abundance of M2-like macrophages affects the response to T cell-engaging immunotherapies in AML, we investigated whether the M2-like macrophage abundance is associated with poor response upon these therapies. However, pre-treatment gene expression data from immunotherapy-treated pediatric AML patients were not available and therefore, we used an immune-related gene expression profiling dataset of pre-treatment BM samples from 30 refractory or relapsed adult AML patients that were treated with flotetuzumab, a bispecific CD3 x CD123 antibody, in the context of a clinical trial (CP-MGD006-01; NCT02152956)[19]. Interestingly, the M2-like macrophage abundance was significantly lower in patients with anti-leukemic activity (n=12) in comparison to non-responders (n=18; two-sided $P < 0.001$; **Fig. 2E**). In fact, the M2-like macrophage abundance outperformed several other known predictors of response to immunotherapy (area under the receiver operating characteristic-curve: 0.852 [95% CI 0.71-0.99], $P = 0.0012$; **Fig. 2F**)[17,20]. In summary, we identified a relatively low abundance of M2-like macrophages in immune-infiltrated samples. In addition, we found that the M2-like macrophage abundance in the BM could be used as a potential biomarker for response to T cell-engaging immunotherapies in AML.

## T cells cluster into spatially organized networks in the bone marrow of pediatric AML

Intriguingly, IHC performed to quantify the T cell infiltration in the BM revealed large networks of T cells in immune-infiltrated samples. Previously, it has been shown in mice that circulating naïve T cells home to the BM upon intravenous antigen administration, where they form dense networks of T cells and subsequently, are activated and differentiated towards effector and memory cells[21]. Therefore, we investigated the spatial organization of T cells in pediatric immune-infiltrated, immune-depleted, and non-leukemic BM samples. T cell networks were defined as at least 10 directly interacting T cells (≤10 µm between adjacent nuclei), to minimize the chance of classifying randomly dispersed T cells as networks (**Fig. 3A**)[22]. Interestingly, T cell networks were detected in both AML groups and in controls, although significantly more frequent in immune-infiltrated samples compared to immune-depleted samples ($P < 0.001$; **Fig. 3B** and **Table S2**). In fact, there was a strong correlation between the level of T cell infiltration and the number of T cell networks, albeit two out of eight immune-infiltrated patients had a relatively low number of networks (n=53; $r = 0.86$ [95% CI: 0.77-0.92], $P < 0.001$; **Fig. 3C**). Also, with respect to the size of T cell networks, immune-infiltrated samples were the only ones with a multitude of large networks (at least 100 directly interacting T cells; **Fig. 3D**). Remarkably, we noticed that in these biopsies, T cell network areas were largely devoid of AML cells, which could indicate local clearance of AML cells (determined using AML immunophenotypic markers; **Fig. 3E-F**)[23]. In contrast, we did not identify such large T cell networks in the BM of immune-depleted samples (**Fig. 3G-H**). Taken together, these data show that spatially organized networks of T cells are widely abundant in pediatric AML patients with an immune-infiltrated BM, potentially reflecting local priming of anti-tumor immunity and/or immune-mediated elimination of AML cells.

## Spatial transcriptomics reveals localized cellular and humoral immunity in *KMT2A*-rearranged patients

Subsequently, we wondered whether these large T cell networks in the BM resemble secondary lymphoid organ-like structures, as seen in solid cancers ('tertiary lymphoid structures', TLSs)[24]. First, we checked whether T cells colocalized with $CD20^+$ B cells, since both T and B cells are the main components of secondary lymphoid organs[25]. Indeed, in four immune-infiltrated pediatric AML BM samples, we detected large aggregates composed of T- and B cells ('lymphoid aggregates'; defined as networks of at least 100 directly interacting T cells that colocalized with a dense core of $CD20^+$ B cells). Interestingly, all four patients had *KMT2A*-rearranged AML. Importantly, these lymphoid aggregates were not classified as malignant upon pathological examination[26]. In fact, these aggregates had a non-trabecular localization, did not contain cells with atypical morphology, and showed a predominance of $CD3^+$ T cells, all features that have been associated with benign BM lymphoid aggregates[26].

In immune-depleted and non-leukemic control samples, we did not detect such lymphoid aggregates. Moreover, in solid cancers, TLSs arise in the context of chronic inflammation[24], which may also have driven the formation of lymphoid aggregates in the BM of immune-infiltrated samples. To test whether lymphoid aggregates in the BM of pediatric AML patients represent structures similar to TLSs, we performed spatial transcriptomics using the GeoMx platform on bone biopsy tissue of two *KMT2A*-rearranged patients that had an immune-infiltrated BM with lymphoid aggregates (**Fig. 4A-B**)[27]. As a control, we used tissue of one *KMT2A*-rearranged patient with an immune-infiltrated BM but without these aggregates (**Fig. 4C**). In total, we successfully sequenced 94 regions: (1) regions that contained lymphoid aggregates (n=20), (2) regions with T cell networks (n=26), and (3) regions that consisted of a mixture of AML-, T-, and B cells ('mixed' regions; n=48). Then, we explored which regions expressed TLS-associated genes using a previously generated TLS-signature (**Fig. 4A-C**)[28]. In general, we observed concordant enrichment of the TLS-signature in areas we designated as regions containing lymphoid aggregates and hence, termed these structures 'TLS-like aggregates' (**Fig. 4A-B**). Surprisingly, one region in the biopsy without lymphoid aggregates was heavily enriched for the TLS-signature, possibly reflecting a forming or disintegrating TLS-like aggregate (**Fig. 4C**).

We next used *SpatialDecon*, a deconvolution approach optimized for spatial transcriptomic data, to examine the abundance of multiple immune and stromal cell types in these TLS-like aggregates[29]. To this end, we used safeTME, a scRNA-seq and flow-sorted bulk RNA-seq based reference profile of microenvironmental cell populations[29]. Importantly, the similarity in cellular composition identified using unsupervised hierarchical clustering (Euclidian distance; complete linkage) was highly concordant with our IHC-based distinction between regions (**Fig. 5A**). Interestingly, TLS-like aggregate regions and T cell networks both showed a significantly higher abundance of memory cytotoxic T cells, potentially because of local cytotoxic T cell priming (**Fig. 5B**)[13]. However, both types of regions also had a significantly higher abundance of Tregs, which may be a limiting factor of anti-tumor immunity (**Fig. 5C**)[30]. Because of this colocalization of cytotoxic T cells with Tregs, we interrogated the functional state of cytotoxic T cells using an additional scRNAseq reference profile specific for activated and resting BM T cells[29]. TLS-like aggregate regions not only had a significantly higher abundance of both activated and resting cytotoxic T cells, but also showed the highest ratio of activated to resting cytotoxic T cells in comparison to T cell network- and mixed regions (mean ratio of 0.72, 0.68, and 0.55, respectively), suggesting that cytotoxic T cells in TLS-like aggregates are present in an activated state despite the presence of Tregs (**Fig. 5D-E** & **Fig. S2B**). Furthermore, the relatively high number of activated T cells may explain the absence of AML cells in these areas. In contrast to the T cell compartment, TLS-like aggregate regions

had a significantly higher abundance of all measured B cell populations in comparison to mixed- and T cell network regions (**Fig. 5F-H**). Notably, differential gene expression analysis between TLS-like aggregate and mixed regions showed upregulation of genes indicative of immunoglobulin class-switching (*IGHG3*, *IGHG4*, *IGHA1*; **Fig. S2A**). Also, we confirmed the enrichment of plasma and/or memory B cells in TLS-like aggregate regions using IHC, together suggesting anti-tumor antibody production in TLS-like aggregate regions (**Fig. 5I**)[31]. Other critical components of the TLSs seen in solid cancers are dendritic cells because of their pivotal role in priming of the immune response[24]. Interestingly, myeloid but not plasmacytoid dendritic cells were significantly enriched in TLS-like aggregate regions in comparison to mixed regions (**Fig. 5I** & **Fig. S2C**). Furthermore, macrophages were significantly enriched in TLS-like aggregate and T cell network regions in comparison to mixed regions, which we validated using IHC (**Fig. 5J&M**). Specifically, TLS-like aggregates and T cell network regions showed a modest decrease in the abundance of M2-like macrophages compared to mixed regions, suggesting that the M1-like macrophage abundance was increased in TLS-like aggregate and T cell network regions (**Fig. 5K)**. In contrast, neutrophils had a significantly higher abundance in mixed regions (**Fig. S2D**).

Finally, since the presence of TLSs, with few exceptions, has been associated with favorable prognosis and response to immunotherapy in solid cancers, we wondered whether the presence of TLS-like aggregates was linked to outcome in patients with AML[24]. Unfortunately, the lack of access to pre-treatment RNA-sequencing data from immunotherapy-treated AML patients precluded investigating whether the presence of TLS-like aggregates is associated with immunotherapy response in AML. As the low number of patients with TLS-like aggregates in our chemotherapy-treated cohort did not allow for robust outcome analyses, we took advantage of publicly available bulk RNA-sequencing data from newly diagnosed pediatric and adult AML patients and used the above-mentioned TLS-signature as a surrogate for the presence of TLS-like aggregates. We found a trend towards improved overall survival for adult AML but not for pediatric AML patients with a TLS-signature score above the median ($P$ = 0.075 and $P$ = 0.53, respectively; **Fig. S3A-B**; TARGET-AML cohort (n=145) and TCGA-cohort (n=140), respectively)[28,32-33]. Collectively, these results suggest that *KMT2A*-rearranged pediatric AML patients with an immune-infiltrated BM may harbor spatially organized areas of cellular and humoral anti-tumor immunity in the BM, which may translate to a positive effect on response upon T cell-engaging immunotherapies[24].

## Discussion

Pediatric cancers are characterized by a relatively low mutational burden and therefore, children are thought to be poor candidates for T cell-engaging immunotherapies[2,3]. This prompted us to perform a multidimensional characterization of the tumor immune

microenvironment in newly diagnosed children with *de novo* AML and non-leukemic controls. We identified a subset of patients with remarkably high T cell infiltration in the BM, dissected the spatial organization of the immune compartment, and for the first time, unraveled the composition of TLS-like aggregates in the BM of AML.

Despite the relatively low mutational burden and the associated poor immunogenicity of pediatric cancers, previous work has shown that considerable variation in immune cell infiltration exists in cancers that are considered to be immunologically 'cold'[4,6]. Indeed, we observed wide variation in T cell infiltration in the BM of pediatric AML patients, including a subset that had remarkably high levels of T cell infiltration. These immune-infiltrated samples showed gene expression suggestive of an enrichment of GZMK$^{+}$ cytotoxic T cells, which has been associated with response to immune checkpoint blockade in adult AML patients[11]. Hence, pediatric AML patients with an immune-infiltrated BM may show increased responses to immune checkpoint inhibitors in comparison to patients with an immune-depleted BM. Specifically, the immune checkpoint receptor genes *TIGIT* and *LAG3* were the most upregulated immune checkpoint genes in immune-infiltrated patients, suggesting that these less conventional checkpoint receptors may prove interesting immunotherapeutic targets in pediatric AML[14,34]. Furthermore, we identified that immune-infiltrated samples harbored a significantly lower abundance of the immunosuppressive M2-like macrophages in comparison to immune-depleted samples. Therefore, repolarizing M2-like macrophages towards an M1-like phenotype could be a suitable immunotherapeutic option in pediatric AML patients with an immune-depleted BM[35]. Of interest, a recent study indicated that M2-like macrophages in the BM of adult AML patients showed increased expression of the immune checkpoints TIGIT and LAG-3 compared to healthy donors, and that TIGIT blockade was able to repolarize these M2-like macrophages to an M1-like phenotype[36]. Thus, TIGIT and LAG-3 blockade may have beneficial effects on both the T cell and macrophage compartment, which encourages further evaluation of these agents in the preclinical setting.

In solid cancers, the importance of the spatial component of the immune response is widely recognized. For instance, in the so-called 'excluded' tumors, an immune response is triggered but not able to invade the tumor bed and hence, associates with poor response to immunotherapy[1]. In hematological malignancies, the spatial organization of the immune response is understudied, while potentially critical to the success of immunotherapeutic interventions. In our study, we identified large aggregates of T- and B cells in the leukemic BM that resembled gene expression characteristics of TLSs[28]. Importantly, pathology examination indicated that the TLS-like aggregates detected in immune-infiltrated pediatric AML samples in our cohort were not of malignant origin. In fact, these aggregates likely arose because of the chronically inflamed tumor microenvironment, as seen with TLSs in solid cancers[24]. In line

with this, we did not detect TLS-like aggregates in the immune-depleted or non-leukemic control samples. Furthermore, we dissected the composition of these TLS-like aggregates in the BM of pediatric AML patients, which turned out to be local hotspots of activated cytotoxic T cells, memory B cells, and plasma cells. Moreover, these hotspots were largely devoid of AML cells despite full-blown leukemia in other areas of the BM. Hence, these data suggest the presence of localized anti-tumor immunity in the BM of AML, which may have profound implications for future immunotherapy approaches. For instance, the increased abundance of plasma cells and the expression of class-switched immunoglobulin genes suggest the production of anti-tumor antibodies, which may lead to novel targets for antibody-based therapies through identification of the respective target antigens[37]. Likewise, the presence of TLS-like aggregates in AML may pave the way for new adoptive cell therapies with tumor-infiltrating T cells, since the T cells primed in these structures are likely to be tumor-reactive[24]. Current immunotherapies may also release the breaks of TLS-like aggregate-associated anti-tumor immunity, as illustrated by the results of a recent clinical trial in advanced soft-tissue sarcoma which showed that patients enrolled based on the presence of TLSs had an overall response rate of 30% to PD-1 blockade, opposed to 2.4% in an unselected cohort[38].

Remarkably, all four patients with TLS-like aggregates in the BM had a *KMT2A*-rearrangement. Although we detected wide variation in T cell infiltration in patients with this cytogenetic alteration, the detection of these aggregates in patients with *KMT2A*-rearranged AML indicates that at least some of these patients, which have relatively poor outcomes upon chemotherapy, may be good candidates for immunotherapy. Furthermore, in an external dataset of chemotherapy-treated adult AML patients, we identified that a high TLS-signature score showed a trend towards better survival, while we did not identify such an association in a large dataset of chemotherapy-treated pediatric AML patients. We speculate that this discrepancy between adult and pediatric AML may be related to differences in the composition of TLS-like aggregates, or to chemotherapy-induced remodeling of these structures, both topics that demand further study[24]. Unfortunately, we did not have access to pre-treatment bone biopsies or RNA-sequencing data from AML patients treated with T cell-engaging immunotherapies and therefore, it was not possible to study the predictive effect of TLS-like aggregates in this context. However, the predictive effect of these structures may easily be studied in both retrospective and future immunotherapy studies. In conclusion, our results suggest the presence of distinct immune phenotypes in the BM of patients with pediatric AML including the presence of TLS-like aggregates in *KMT2A*-rearranged AML, suggesting that a subset of children with AML may benefit from T cell-engaging immunotherapies, and which encourages further study of these lymphoid structures in the BM in the context of immunotherapy in AML.

## Methods

### Ethical regulation

This study complies with all relevant ethical regulations and was approved by the Institutional Review Board of the Princess Máxima Center for Pediatric Oncology (PMCLAB2021.207 & PMCLAB2021.238) and the Scientific Committee of the Dutch Nationwide Pathology Databank (PALGA: lzv2021-82)[39]. All patients treated at the Princess Máxima Center provided written consent for banking and research use of these specimens, according to the Declaration of Helsinki. Bone biopsy tissues acquired from external biobanks (n=28) were leftover material from standard care procedures and therefore, no informed consent was acquired, according to Dutch legislation and the code of conduct of the Committee on Regulation of Health Research (COREON).

### Human patient samples

FFPE bone biopsies taken from the crista of children with treatment-naïve *de novo* AML were obtained from the Princess Máxima Center Biobank (n=15) and biobanks of 10 other Dutch hospitals (n=28), mediated by the Dutch National Tissue Portal. As controls, FFPE bone biopsies of age- and sex-matched children with treatment-naïve early-stage rhabdomyosarcoma were obtained from the Princess Máxima Center Biobank (n=10; non-leukemic controls). An experienced hemato-onco pathologist confirmed that these control biopsies resembled normal hematopoiesis and that there was no malignancy infiltrating the BM.

### Immunohistochemistry staining and digital image analysis

Bone biopsies were cut into consecutive 4 µm sections and stained with hematoxylin and eosin (H&E). Conventional IHC was performed for CD3, CD3-CD4 (duplex), CD8, CD20, CD34, CD117, CD15, and IgM-IgG (duplex) using a Ventana Benchmark Ultra (Roche, Basel, Switzerland) automated staining instrument according to manufacturers' recommendations. A list of antibodies and suppliers is available in **Table S3**. Digital scans of stained slides were obtained using a NanoZoomer scanner (Hamamatsu, Shizuoka, Japan). On 4 µm sections from three *KMT2A*-rearranged pediatric AML patients with an immune-infiltrated BM, we applied the FixVUE APC™ Kit (Ultivue Inc. Cambridge, MA, USA; CD20, CD68/CD163 cocktail, CD11c, and MHC-II) using the antibody conjugated DNA-barcoded multiplexed immunofluorescence method, as previously described[40]. The staining was performed on the BOND RX (Leica Biosystems, Wetzlar, Germany). To acquire an H&E staining on the same slide, the fluorescently labelled slides were soaked in PBS until the coverslips could be removed, and a standard H&E stain was performed using an Epredia Gemini (Epredia,

Portsmouth, UK). Digital immunofluorescence and brightfield images were scanned on a Zeiss Axioscan Z1 (ZEISS, Oberkochen, Germany) and stacked with Ultivue's UltiStacker software. Whole-slide digital image analysis was performed in QuPath (V.0.3.2)[41]. Inside QuPath, the deep learning-based cell segmentation tool StarDist and the machine learning-based Random Trees classifier were used to quantify the number of positive cells per $mm^2$ [42]. T cell networks were defined as at least 10 directly interacting $CD3^+$ T cells (≤ 10 µm between adjacent nuclei), detected using Delaunay Triangulation, and normalized per 10 $cm^2$ [42-43]. Large T cell networks of at least 100 directly interacting T cells that colocalized with a dense core of $CD20^+$ B cells were classified as lymphoid aggregates.

**Immune-related gene expression profiling**

Four consecutive sections of 10 µm from 5 immune-infiltrated and 18 immune-depleted FFPE bone biopsies (the non-leukemic controls' median value of cytotoxic T cells was used as the cut-off value) from a cytogenetically representative cohort of pediatric AML patients were used to isolate RNA and to perform immune-related gene expression profiling with the 770-gene PanCancer IO 360 panel, as previously described (NanoString, Seattle, WA, USA)[19,44]. After passing quality control, raw data were normalized using ROSALIND® according to Nanostring's recommendations (https://rosalind.bio/; San Diego, CA, USA). Normalized data were uploaded to the online iDEP platform and differentially expressed genes between immune-infiltrated and immune-depleted samples were identified using *DEseq2* with a false-discovery rate (FDR) cut-off of 0.05 and a minimum fold change of 2 (integrative Differential Expression and Pathway analysis; http://bioinformatics.sdstate.edu/idep96/; V.0.96)[45]. Pathway analysis was performed using parametric gene set enrichment analysis with the GO Biological Processes gene set with an FDR of 0.05[46,47]. The abundance of M2-like macrophages was estimated using a published gene signature of M2-like macrophages compared to M1-like macrophages, inside the TIDE environment (tide.dfci.harvard.edu/)[17,48]. Similarly, the T cell inflamed gene expression profile, the CD8-, IFN-*γ*-, and TIDE scores were all calculated using TIDE.

**GeoMx Digital Spatial Profiling**

5 µm thick FFPE bone biopsy sections from three *KMT2A*-rearranged pediatric AML patients with an immune-infiltrated BM were placed on the same slide and prepared for GeoMx Digital Spatial Profiling (DSP; NanoString), as previously described[27]. Slides were simultaneously incubated with immunofluorescent antibodies and GeoMx Whole Transcriptome Atlas profiling reagents. SYTO13 (S7575, Thermo Fisher,) was used for identification of nuclei, CD45 (NBP2-34528, Novus) for leukocytes, and CD3 (NBP2-54392AF647, Novus) for T cells. Stained slides were loaded onto the GeoMx instrument and scanned. Regions of interest

(ROIs) were selected using the above-mentioned antibodies in combination with overlayed images of CD20, CD34, CD3-CD4 (duplex), and CD117 (IHC). Then, UV-photocleaved oligonucleotides were collected in separate wells and sequenced on the Nextseq2000 (Illumina, San Diego, CA, USA). In total, we successfully sequenced 94 regions (one failed quality control) with on average 273 cells per region (range: 156 to 778 cells). Raw data were normalized using Quartile 3 count (Q3) normalization in R (V.4.2.1) as per NanoString's recommendations (code is available in the vignette of the *Geomxtools* package). The expression of the TLS-signature as described by Meylan et al. was plotted in R on the scanned image using *SpatialOmicsOverlay*[28]. Spatial Deconvolution was performed in the GeoMx DSP Analysis Suite using both the safeTME and healthy adult BM T cell reference profiles (*SpatialDecon* package; cell reference profiles are available via https://github.com/Nanostring-Biostats/CellProfileLibrary)[29]. Differential gene expression analysis between regions was performed using a linear mixed-effects model including random slope to correct for the fact that multiple regions come from the same biopsy, and the FDR method (code: *Geomxtools* package; minimum fold change of 2).

**External pediatric and adult AML datasets**

Single-cell RNA-sequencing (scRNAseq) data from 8 newly diagnosed pediatric AML patients were re-analyzed for cell-type specific *PDCD1*, *CTLA4*, *TIGIT*, and *LAG3* expression using the Tumor Immune Single-cell Hub[14,49]. Immune-related gene expression data (PanCancer IO 360 panel) from pre-treatment BM samples from 30 relapsed or refractory adult AML patients that were treated with flotetuzumab in the context of the CP-MGD006-01 clinical trial (NCT02152956) were kindly provided by Professor Sergio Rutella (Nottingham Trent University, England) and dr. Patrick Kaminker (MacroGenics, Rockville, MD, USA) and analyzed as described above. The association between the TLS-signature score[28] (averaged expression of normalized counts) and overall survival of 145 and 140 newly diagnosed *de novo* pediatric and adult AML patients was evaluated using the online platform SurvivalGenie, respectively (TARGET-AML and TCGA-AML cohorts; https://bbisr.shinyapps.winship.emory.edu/SurvivalGenie/)[32-33,50].

**Statistical analyses**

Statistical analyses were performed with GraphPad Prism V.9.3.0 (GraphPad Software, LA Jolla, CA, USA). Time to event analyses were performed with SurvivalGenie[50]. Differences between two independent groups were compared using the Mann-Whitney test. The correlation between two variables was evaluated using Spearman's *r*. To measure the area under the receiver operating characteristic curve, we employed the Wilson-Brown method. To estimate the survival from diagnosis, the Kaplan-Meier's methodology was employed. To

assess the difference between survival estimates in different groups, the log rank test was used. In case of multiple comparisons and no Gaussian distribution of residuals, we employed the Kruskal-Wallis test followed by Dunn's test for multiple comparisons including a Bonferroni correction. Hence for the multiple testing, $P<0.01$ was considered statistically significant in these comparisons. For all the other comparisons, $P<0.05$ was considered statistically significant.

**Data availability**

Sequencing data can be accessed from the Gene Expression Omnibus (nCounter data: GSEXXX; GeoMx data: GSEXXX; both normalized counts [GSE IDs will be available upon approval]) and from the European Genome-phenome Archive (EGA) database (https://ega-archive.org/studies/EGAXXX; raw nCounter and GeoMx data [idem]).

**Acknowledgements**

We would like to thank the staff of the University Medical Center Utrecht Tissue Facility for their excellent immunohistochemistry service (Domenico Castigliego, Petra van der Weide, Petra van der Kraak, Karina Timmer, Sven van Kempen), and the team at Utrecht Sequencing Facility for performing the NanoString experiments (nCounter and GeoMx) and for providing assistance with data-analysis (dr. Ies Nijman, Robin Geene, Pim Kloosterman). We are grateful to Professor Sergio Rutella (Notthingham Trent University) and dr. Patrick Kaminker (MacroGenics) for providing us with immune-related gene expression data from immunotherapy-treated adult AML samples. Dr. Ivette Deckers and dr. Annette Gijsbers (PALGA) performed essential work for the acquisition of bone biopsies from other hospitals. From the Princess Máxima Center for Pediatric Oncology, prof. dr. Gertjan Kaspers and dr. Bianca Goemans aided with identifying potential patients, the biobank staff (Jantien Woudstra, Marion Koopmans, dr. Edwin Sonneveld) helped to identify patient material, and Arie Maat aided with the sectioning of bone biopsy sections. Also, we would like to thank dr. Caroline Lindemans, members from the Heidenreich group (dr. Katarzyna Szoltysek, dr. Farnaz Barneh, dr. Mauricio Ferrao-Blanco, Elizabeth Schweighart, Nina van der Wilt), the Van Heesch group (dr. Ana Pinheiro-Lopes), and the single-cell sequencing facility (dr. Lindy Visser) at the Princess Máxima Center for Pediatric Oncology for carefully reading the manuscript and/or fruitful discussions. This work has been funded in part by a KIKA (329) program grant to O.H. Figure 1A and 3A have been created using BioRender.com.

**Author contributions**

Conceptualization: J.B.K, I.W., M.A.V., S.N., M.B., C.M.Z., O.H. Methodology: J.B.K, I.W., M.A.V., M.F., S.N., M.B., C.M.Z., O.H. Data acquisition: J.B.K., M.A.V., H.G.-K., R.M. Data

analysis and interpretation: J.B.K., I.W., A.P. Writing – Original Draft: J.B.K.; Writing – Reviewing & Editing: all authors; Supervision: S.N., M.B., C.M.Z., O.H.

## References


1. Bruni D, Angell HK, Galon J. The immune contexture and Immunoscore in cancer prognosis and therapeutic efficacy. *Nat Rev Cancer*. 2020;20(11):662-680.
2. Majzner RG, Heitzeneder S, Mackall CL. Harnessing the Immunotherapy Revolution for the Treatment of Childhood Cancers. *Cancer Cell*. 2017;31(4):476-485.
3. Pfister SM, Reyes-Múgica M, Chan JKC, Hasle H, Lazar AJ, Rossi S, et al. A Summary of the Inaugural WHO Classification of Pediatric Tumors: Transitioning from the Optical into the Molecular Era. *Cancer Discov*. 2022;12(2):331-355.
4. Dufva O, Pölönen P, Brück O, Keränen MAI, Klievink J, Mehtonen J, et al. Immunogenomic Landscape of Hematological Malignancies. *Cancer Cell*. 2020;38(3):380-399.e13.
5. Serroukh Y, Hébert J, Busque L, Mercier F, Rudd CE, Assouline S, et al. Blasts in context: the impact of the immune environment on acute myeloid leukemia prognosis and treatment. *Blood Rev*. 2023;57:100991.
6. Gröbner SN, Worst BC, Weischenfeldt J, Buchhalter I, Kleinheinz K, Rudneva VA, et al. The landscape of genomic alterations across childhood cancers. *Nature*. 2018;555(7696):321-327.
7. Vadakekolathu J, Lai C, Reeder S, Church SE, Hood T, Lourdusamy A, et al. TP53 abnormalities correlate with immune infiltration and associate with response to flotetuzumab immunotherapy in AML. *Blood Adv*. 2020;4(20):5011-5024.
8. Koedijk JB, van der Werf I, Calkoen FG, Nierkens S, Kaspers GJL, Zwaan CM, et al. Paving the Way for Immunotherapy in Pediatric Acute Myeloid Leukemia: Current Knowledge and the Way Forward. *Cancers (Basel)*. 2021;13(17):4364.
9. Wellenstein MD, de Visser KE. Cancer-Cell-Intrinsic Mechanisms Shaping the Tumor Immune Landscape. *Immunity*. 2018;48(3):399-416.
10. de Rooij JD, Zwaan CM, van den Heuvel-Eibrink M. Pediatric AML: From Biology to Clinical Management. *J Clin Med*. 2015;4(1):127-149.
11. Abbas HA, Hao D, Tomczak K, Barrodia P, Seon Im J, Reville PK, et al. Single cell T cell landscape and T cell receptor repertoire profiling of AML in context of PD-1 blockade therapy. *Nat Commun*. 2021;12(1):6071.
12. Ye Q, Song DG, Poussin M, Yamamoto T, Best A, Li C, et al. CD137 accurately identifies and enriches for naturally occurring tumor-reactive T cells in tumor. *Clin Cancer Res*. 2014;20(1):44-55.
13. Philip M, Schietinger A. $CD8^+$ T cell differentiation and dysfunction in cancer. *Nat Rev Immunol*. 2022;22(4):209-223.
14. Bailur JK, McCachren SS, Pendleton K, Vasquez JC, Seo Lim H, Duffy A, et al. Risk-associated alterations in marrow T cells in pediatric leukemia. *JCI Insight*. 2020;5(16):e140179.
15. House IG, Savas P, Lai J, Chen AXY, Oliver AJ, Teo ZL, et al. Macrophage-Derived CXCL9 and CXCL10 Are Required for Antitumor Immune Responses Following Immune Checkpoint Blockade. *Clin Cancer Res*. 2020;26(2):487-504.
16. Italiani P, Boraschi D. From Monocytes to M1/M2 Macrophages: Phenotypical vs. Functional Differentiation. *Front Immunol*. 2014;5:514.
17. Jiang P, Gu S, Pan D, Fu J, Sahu A, Hu X, et al. Signatures of T cell dysfunction and exclusion predict cancer immunotherapy response. *Nat Med*. 2018;24(10):1550-1558.

18. Mussai F, De Santo C, Abu-Dayyeh I, Booth S, Quek L, McEwen-Smith RM, et al. Acute myeloid leukemia creates an arginase-dependent immunosuppressive microenvironment. *Blood*. 2013;122(5):749-758.
19. Vadakekolathu J, Minden MD, Hood T, Church SE, Reeder S, Altmann H, et al. Immune landscapes predict chemotherapy resistance and immunotherapy response in acute myeloid leukemia. *Sci Transl Med*. 2020;12(546):eaaz0463.
20. Ayers M, Lunceford J, Nebozhyn M, Murphy E, Loboda A, Kaufman DR, et al. IFN-γ-related mRNA profile predicts clinical response to PD-1 blockade. *J Clin Invest*. 2017;127(8):2930-2940.
21. Feuerer M, Beckhove P, Garbi N, Mahnke Y, Limmer A, Hommel M, et al. Bone marrow as a priming site for T-cell responses to blood-borne antigen. *Nat Med*. 2003;9(9):1151-1157.
22. Gaglia G, Burger M, Ritch CC, Rammos D, Dai Y, Crossland GE, et al. Lymphocyte networks are dynamic communities in the immunoregulatory landscape of lung adenocarcinoma. *bioRxiv*. 2022-08.
23. Pospori C, Grey W, Gonzalez Anton S, Gibson S, Georgiou C, Birch F, et al. Dynamic regulation of hierarchical heterogeneity in acute myeloid leukemia serves as a tumor immunoevasion mechanism. bioRxiv. 2020-12.
24. Schumacher TN, Thommen DS. Tertiary lymphoid structures in cancer. *Science*. 2022;375(6576):eabf9419.
25. Ruddle NH, Akirav EM. Secondary lymphoid organs: responding to genetic and environmental cues in ontogeny and the immune response. *J Immunol*. 2009;183(4):2205-2212.
26. Maccio U, Rets AV. Lymphoid aggregates in bone marrow: a diagnostic pitfall. *J Clin Pathol*. 2022;75(12):807-814.
27. Merritt CR, Ong GT, Church SE, Barker K, Danaher P, Geiss G, et al. Multiplex digital spatial profiling of proteins and RNA in fixed tissue. *Nat Biotechnol*. 2020;38(5):586-599.
28. Meylan M, Petitprez F, Becht E, Bougoüin A, Pupier G, Calvez A, et al. Tertiary lymphoid structures generate and propagate anti-tumor antibody-producing plasma cells in renal cell cancer. *Immunity*. S2022;55(3):527-541.e5.
29. Danaher P, Kim Y, Nelson B, Griswold M, Yang Z, Piazza E, et al. Advances in mixed cell deconvolution enable quantification of cell types in spatial transcriptomic data. *Nat Commun*. 2022;13(1):385
30. Joshi NS, Akama-Garren EH, Lu Y, Lee D-Y, Chang GP, Li A, et al. Regulatory T Cells in Tumor-Associated Tertiary Lymphoid Structures Suppress Anti-tumor T Cell Responses. *Immunity*. 2015;43(3):579-590.
31. Akkaya M, Kwak K, Pierce SK. B cell memory: building two walls of protection against pathogens. *Nat Rev Immunol*. 2020;20(4):229-238.
32. Bolouri H, Farrar JE, Triche T Jr, Ries RE, Lim EL, Alonzo TA, et al. The molecular landscape of pediatric acute myeloid leukemia reveals recurrent structural alterations and age-specific mutational interactions. *Nat Med*. 2018;24(1):103-112.
33. Cancer Genome Atlas Research Network, Ley TJ, Miller C, Ding L, Raphael BJ, Mungall AJ, et al. Genomic and epigenomic landscapes of adult de novo acute myeloid leukemia. *N Engl J Med*. 2013;368(22):2059-2074.
34. Lasry A, Nadorp B, Fornerod M, Nicolet D, Wu H, Walker CJ, et al. An inflammatory state remodels the immune microenvironment and improves risk stratification in acute myeloid leukemia. *Nat Cancer*. 2023;4(1):27-42.

35. Li W, Wang F, Guo R, Bian Z, Song Y. Targeting macrophages in hematological malignancies: recent advances and future directions. *J Hematol Oncol*. 2022;15(1):110.
36. Brauneck F, Fischer B, Witt M, Muschhammer J, Oelrich J, Henrique da Costa Avelar P, et al. TIGIT blockade repolarizes AML-associated TIGIT$^+$ M2 macrophages to an M1 phenotype and increases CD47-mediated phagocytosis. *J Immunother Cancer*. 2022;10(12):e004794.
37. Fridman WH, Meylan M, Petitprez F, Sun CM, Italiano A, Sautès-Fridman C. B cells and tertiary lymphoid structures as determinants of tumour immune contexture and clinical outcome. *Nat Rev Clin Oncol*. 2022;19(7):441-457.
38. Italiano A, Bessede A, Pulido M, Bompas E, Piperno-Neumann S, Chevreau C, et al. Pembrolizumab in soft-tissue sarcomas with tertiary lymphoid structures: a phase 2 PEMBROSARC trial cohort. *Nat Med*. 2022;28(6):1199-1206.
39. Casparie M, Tiebosch AT, Burger G, Blauwgeers H, van de Pol A, van Krieken JHJM, et al. Pathology databanking and biobanking in The Netherlands, a central role for PALGA, the nationwide histopathology and cytopathology data network and archive. *Cell Oncol*. 2007;29(1):19-24.
40. Manesse M, Patel KK, Bobrow M, Downing SR. The InSituPlex® Staining Method for Multiplexed Immunofluorescence Cell Phenotyping and Spatial Profiling of Tumor FFPE Samples. *Methods Mol Biol*. 2020;2055:585-592.
41. Bankhead P, Loughrey MB, Fernández JA, Dombrowski Y, McArt DG, Dunne PD, et al. QuPath: Open source software for digital pathology image analysis. *Sci Rep*. 2017;7(1):16878.
42. Schmidt U, Weigert M, Broaddus C, Myers G. Cell detection with star-convex polygons. *International Conference on Medical Image Computing and Computer-Assisted Intervention*. 2018;265-273.
43. Delaunay B. Sur la sphère vide. *Bull. Acad. Sci. URSS*. 1934:793–800.
44. Danaher P, Warren S, Dennis L, D'Amico L, White A, Disis ML, et al. Gene expression markers of Tumor Infiltrating Leukocytes. *J Immunother Cancer*. 2017;5:18.
45. Ge SX, Son EW, Yao R. iDEP: an integrated web application for differential expression and pathway analysis of RNA-Seq data. *BMC Bioinformatics*. 2018;19(1):534.
46. Ashburner M, Ball CA, Blake JA, Botstein D, Butler H, Cherry JM, et al. Gene ontology: tool for the unification of biology. The Gene Ontology Consortium. *Nat Genet*. 2000;25(1):25-29.
47. Gene Ontology Consortium. The Gene Ontology resource: enriching a GOld mine. *Nucleic Acids Res*. 2021;49(D1):D325-D334.
48. Beyer M, Mallmann MR, Xue J, Staratcheck-Jox A, Vorholt D, Krebs W, et al. High-resolution transcriptome of human macrophages. *PLoS One*. 2012;7(9):e45466.
49. Sun D, Wang J, Han Y, Dong X, Ge J, Zheng R, et al. TISCH: a comprehensive web resource enabling interactive single-cell transcriptome visualization of tumor microenvironment. *Nucleic Acids Res*. 2021;49(D1):D1420-D1430.
50. Dwivedi B, Mumme H, Satpathy S, Bhasin SS, Bhasin M. Survival Genie, a web platform for survival analysis across pediatric and adult cancers. *Sci Rep*. 2022;12(1):3069

## Figure Legends

**Figure 1. Spatial analysis of the bone marrow immune microenvironment in pediatric AML and non-leukemic controls.**

(A) Schematic overview of the study population, used techniques, and the digital image analysis pipeline. (B-C) Representative bone biopsy images acquired from a treatment-naïve pediatric AML patient (B) and non-leukemic control (C) showing H&E staining, $CD3^+$ T cells (CD3 in brown), and $CD8^+$ T cells (CD8 in brown). White lobules indicate adipocytes. (D-E) Comparison of the normalized abundance of $CD3^+$ T cells (D) and $CD8^+$ T cells (E) in the BM between pediatric AML patients and non-leukemic controls. (F-G) Normalized abundance of $CD3^+$ T cells (F) and $CD8^+$ T cells (G) per cytogenetic pediatric AML subgroup. 'Normal' indicates normal karyotype, while 'Others' is a merge of cytogenetic abnormalities different from the four defined cytogenetic subgroups.

**Figure 2. Transcriptional differences between immune-infiltrated and immune-depleted pediatric AML samples.**

(A) Volcano plot of differentially expressed genes between immune-infiltrated and immune-depleted pediatric AML BM samples, identified using *DEseq2* with an FDR cut-off of 0.05 and minimum fold change (FC) of 2. (B) Parametric gene set enrichment analysis of differentially expressed genes between immune-infiltrated (orange) and immune-depleted samples (blue) using the GO Biological Processes gene set with an FDR cut-off of 0.05. Values in front of the biological processes indicate *P* values. (C) Correlation plot of the inverse correlation between the M2-like macrophage abundance and the normalized number of $CD3^+$ T cells, calculated using Spearman correlation. (D-E) Comparison of the M2-like macrophage abundance between immune-infiltrated (n=5) and immune-depleted (n=18) BM samples (D) and between BM samples of refractory or relapsed (R/R) adult AML patients with anti-leukemic activity (ALA) or non-responders (NR) to treatment with the bispecific antibody flotetuzumab (E). (F) Area under the receiver operating characteristic curves measuring the predictive ability of the M2-like macrophage abundance (black), T cell inflamed gene expression profile (GEP; pink), CD8 score (blue), IFN-*γ* score (green), and the tumor immune dysfunction and exclusion score (TIDE; orange) in pre-treatment R/R adult AML samples for response to flotetuzumab.

**Figure 3. Immune-infiltrated pediatric AML samples harbor an increased abundance of spatially organized T cell networks.**

(A) Illustration of the identification of directly interacting T cells (above) and T cell networks (below) using Delaunay Triangulation. (B) Comparison of the normalized abundance of T cell

networks between immune-infiltrated, immune-depleted, and non-leukemic control samples. (C) Correlation plot of the positive correlation between the normalized number of $CD3^+$ T cells and the normalized number of T cell networks in both AML and non-leukemic control samples (n=53), calculated using Spearman correlation. (D) Comparison of the number of T cell networks with at least 100 T cells/network between immune-infiltrated, immune-depleted, and non-leukemic control samples. (E-F) Representative images of an immune-infiltrated pediatric AML BM sample with multiple large T cell clusters (>100 T cells; CD3 in brown; E) that are largely devoid of AML cells (CD117 in brown, patient-specific AML immunophenotypic marker; F). (G-H). Representative images of an immune-depleted pediatric AML BM sample without T cell clusters (CD3 in brown; G) and widely dispersed AML cells (CD117 in brown; patient-specific AML immunophenotypic marker; H).

**Figure 4. Spatial transcriptomics reveals gene expression characteristics of tertiary lymphoid structures in *KMT2A*-rearranged immune-infiltrated pediatric AML samples.**

(A-C) Images of the bone biopsy sections that show the expression levels of a previously published TLS-signature in distinct regions of two lymphoid aggregate (LA)-positive (A+B) *KMT2A*-rearranged immune-infiltrated pediatric AML samples and one LA-negative (C) *KMT2A*-rearranged immune-infiltrated pediatric AML sample, next to immunohistochemistry-based images of $CD3^+$ T cells, $CD20^+$ B cells, and $CD117^+$ (A+C) or $CD4^+$ (B) AML cells. Orange arrows indicate LA-containing regions.

**Figure 5. Spatial deconvolution identifies localized cellular and humoral immunity in *KMT2A*-rearranged immune-infiltrated pediatric AML samples.**

(A) Dendrogram and bar plot of absolute immune- and stromal-cell abundance scores, calculated by applying the *SpatialDecon* algorithm to spatial transcriptomic data from three *KMT2A*-rearranged immune-infiltrated pediatric AML BM samples. Regions are divided in separate clusters based on similarity (unsupervised hierarchical clustering; Euclidian distance; complete linkage). The legend on the right indicates which type of cell is shown in the bar plot and for which type of region the cell composition is shown. (B-K) Comparisons of the abundance scores of several immune- and stromal cell types between mixed regions (n=48), T cell network regions (n=26), and TLS-like aggregate regions (n=20). Tregs indicates regulatory T cells, and DCs indicate dendritic cells. (I) Whole-slide bone biopsy image with a CD3 stain (brown) for T cells (above), and a magnified image illustrating the presence of $IgM^+$- (brown) and $IgG^+$-cells (purple) in the T cell rich area that is part of an TLS-like aggregate. (M) Magnifications of the T cell rich area shown in the whole-slide image shown in Figure I, showing the presence of $CD11c^+$ $CD68/CD163^+$ macrophages (red arrows) in the TLS-like aggregate region.

# SUPPLEMENTARY INFORMATION

## Spatial analysis reveals distinct immune phenotypes and tertiary lymphoid structure-like aggregates in pediatric acute myeloid leukemia

Joost B. Koedijk[1,2], Inge van der Werf[1,3], Marijn A. Vermeulen[1], Alicia Perzolli[1,2], Marta Fiocco[1,4,5], Hester A. de Groot-Kruseman[1], Rubina Moeniralam[1], Stefan Nierkens[1,6], Mirjam E. Belderbos[1], C. Michel Zwaan[1,2#], Olaf Heidenreich[1,7#*]

**Supplementary Table 1.** Patient characteristics from 43 treatment-naïve pediatric patients with AML and 10 treatment-naïve non-leukemic controls.

| ID | Sex | %BM Myelo-blasts | FAB | Cytogenetic alterations | Molecular aberrations | Immune infiltration | GEP + Spatial Tx |
|---|---|---|---|---|---|---|---|
| AML1 | male | 32 | M2 | NA | NA | Infiltrated | GEP |
| AML2 | female | 51 | M5 | KMT2Ar | none | Infiltrated | GEP + Spatial Tx |
| AML3 | male | NA | NA | KMT2Ar | none | Infiltrated | GEP |
| AML4 | male | 55 | NA | KMT2Ar | none | Infiltrated | GEP |
| AML5 | male | 28 | NA | KMT2Ar, Trisomy-8 | none | Infiltrated | Spatial Tx |
| AML6 | male | 44 | NA | KMT2Ar | none | Infiltrated | GEP + Spatial Tx |
| AML7 | male | 39 | NA | inv(16) | none | Infiltrated | |
| AML8 | male | 81 | NA | t(8;21), 8q-deletion, Y-chromosome deletion | EXT1mut + RAD21mut | Infiltrated | |
| AML9 | male | 63 | NA | KMT2Ar | none | Depleted | |
| AML10 | male | 81 | NA | KMT2Ar | none | Depleted | |
| AML11 | male | 73 | M5 | inv(16) | none | Depleted | |
| AML12 | male | 77 | M2 | t(8;21) | none | Depleted | GEP |

| | | | | | | | |
|---|---|---|---|---|---|---|---|
| AML13 | female | NA | NA | Normal karyotype | NPM1mut + WT-1mut | Depleted | GEP |
| AML14 | male | 50 | M2 | t(8;21) | none | Depleted | |
| AML15 | female | 14 | M6 | NA | NA | Depleted | |
| AML16 | male | 88 | M1 | t(8;21) | none | Depleted | GEP |
| AML17 | female | 31 | M0 | Normal karyotype | none | Depleted | |
| AML18 | male | 10 | M7 | NA | NA | Depleted | |
| AML19 | male | NA | M5 | NA | NA | Depleted | |
| AML20 | female | NA | M6 | NA | NA | Depleted | |
| AML21 | female | 72 | M4 | Monosomy-7 | none | Depleted | GEP |
| AML22 | male | 94 | M5 | KMT2Ar | none | Depleted | GEP |
| AML23 | male | 98 | M5 | KMT2Ar | none | Depleted | GEP |
| AML24 | female | 20 | NA | NA | NA | Depleted | GEP |
| AML25 | male | 8 | M7 | Trisomy-8 | none | Depleted | GEP |
| AML26 | male | 80 | M5 | KMT2Ar | none | Depleted | GEP |
| AML27 | male | 36 | M2 | t(8;21) | WT-1mut | Depleted | GEP |
| AML28 | female | 69 | NA | KMT2Ar | none | Depleted | GEP |
| AML29 | male | 45 | M2 | NA | NA | Depleted | GEP |
| AML30 | male | 39 | M2 | NA | NA | Depleted | GEP |
| AML31 | female | NA | NA | NA | NA | Depleted | |
| AML32 | female | 38 | NA | inv(16) | none | Depleted | GEP |
| AML33 | female | 34 | NA | Normal karyotype | NPM1mut | Depleted | GEP |
| AML34 | male | NA | NA | Normal karyotype | FLT3-ITDmut | Depleted | GEP |
| AML35 | male | 92 | M5 | KMT2Ar | none | Depleted | |
| AML36 | female | 90 | M5 | KMT2Ar | none | Depleted | |
| AML37 | male | 32 | NA | 9q-deletion | none | Depleted | |
| AML38 | male | 18 | NA | Normal karyotype | none | Depleted | |
| AML39 | male | 0 | NA | Normal karyotype | NPM1mut | Depleted | |

| | | | | | | | |
|---|---|---|---|---|---|---|---|
| AML40 | male | 12 | NA | t(6;9) | WT1mut + NRASmut | Depleted | |
| AML41 | female | 5 | NA | t(5;11) | none | Depleted | |
| AML42 | male | 63 | NA | Monosomy-7, gain chromosome -13 | TP53mut, RUNX1mut, SUZ12mut | Depleted | GEP |
| AML43 | male | 92 | M5 | KMT2Ar | NRASmut | Depleted | GEP |
| CTRL1 | male | 1 | Not applicable | | | | |
| CTRL2 | female | 0 | Not applicable | | | | |
| CTRL3 | female | 1 | Not applicable | | | | |
| CTRL4 | male | 2 | Not applicable | | | | |
| CTRL5 | female | 3 | Not applicable | | | | |
| CTRL6 | male | 1 | Not applicable | | | | |
| CTRL7 | male | 1 | Not applicable | | | | |
| CTRL8 | male | 0 | Not applicable | | | | |
| CTRL9 | male | 2 | Not applicable | | | | |
| CTRL10 | female | 1 | Not applicable | | | | |

AML: acute myeloid leukemia; BM: bone marrow; CTRL: non-leukemic control; dx: diagnosis; FAB: French-American-British (classification); GEP: gene expression profiling; KMT2Ar: KMT2A-rearranged; mut: mutation; NA: not available; Spatial Tx: spatial transcriptomics.

**Supplementary Table 2.** Number of T cell networks and TLS-like aggregates for each patient.

| | | **T cell network number (by size)** | | | | |
|---|---|---|---|---|---|---|
| **ID** | **Immune infiltration** | **10-30 cells** | **31-99 cells** | **100-500 cells** | **>500 cells** | **TLS-like aggregates** |
| AML1 | Infiltrated | 161 | 30 | 11 | 1 | NA |
| AML2 | Infiltrated | 191 | 57 | 15 | 8 | 6 |
| AML3 | Infiltrated | 473 | 62 | 11 | 0 | 11 |
| AML4 | Infiltrated | 92 | 11 | 1 | 0 | 1 |
| AML5 | Infiltrated | 22 | 1 | 0 | 0 | 0 |
| AML6 | Infiltrated | 320 | 48 | 7 | 1 | 4 |
| AML7 | Infiltrated | 138 | 2 | 0 | 0 | 0 |
| AML8 | Infiltrated | 18 | 0 | 0 | 0 | 0 |
| AML9 | Depleted | 541 | 61 | 0 | 0 | 0 |
| AML10 | Depleted | 242 | 9 | 0 | 0 | 0 |
| AML11 | Depleted | 0 | 0 | 0 | 0 | 0 |

| | | | | | | |
|---|---|---|---|---|---|---|
| AML12 | Depleted | 0 | 0 | 0 | 0 | 0 |
| AML13 | Depleted | 1 | 1 | 0 | 0 | 0 |
| AML14 | Depleted | 0 | 0 | 0 | 0 | 0 |
| AML15 | Depleted | 5 | 0 | 0 | 0 | 0 |
| AML16 | Depleted | 3 | 0 | 0 | 0 | 0 |
| AML17 | Depleted | 3 | 0 | 0 | 0 | 0 |
| AML18 | Depleted | 1 | 0 | 0 | 0 | 0 |
| AML19 | Depleted | 0 | 0 | 0 | 0 | 0 |
| AML20 | Depleted | 3 | 0 | 0 | 0 | 0 |
| AML21 | Depleted | 0 | 0 | 0 | 0 | 0 |
| AML22 | Depleted | 6 | 0 | 0 | 0 | 0 |
| AML23 | Depleted | 29 | 0 | 0 | 0 | 0 |
| AML24 | Depleted | 82 | 4 | 1 | 0 | NA |
| AML25 | Depleted | 4 | 0 | 0 | 0 | 0 |
| AML26 | Depleted | 1 | 0 | 0 | 0 | 0 |
| AML27 | Depleted | 1 | 0 | 0 | 0 | 0 |
| AML28 | Depleted | 30 | 0 | 0 | 0 | 0 |
| AML29 | Depleted | 8 | 1 | 0 | 0 | 0 |
| AML30 | Depleted | 10 | 0 | 1 | 0 | 1 |
| AML31 | Depleted | 6 | 0 | 0 | 0 | 0 |
| AML32 | Depleted | 0 | 0 | 0 | 0 | 0 |
| AML33 | Depleted | 0 | 0 | 0 | 0 | 0 |
| AML34 | Depleted | 7 | 0 | 0 | 0 | 0 |
| AML35 | Depleted | 27 | 1 | 0 | 0 | 0 |
| AML36 | Depleted | 0 | 0 | 0 | 0 | 0 |
| AML37 | Depleted | 2 | 1 | 0 | 0 | 0 |
| AML38 | Depleted | 0 | 0 | 0 | 0 | 0 |
| AML39 | Depleted | 19 | 1 | 0 | 0 | 0 |
| AML40 | Depleted | 5 | 0 | 0 | 0 | 0 |
| AML41 | Depleted | 51 | 7 | 0 | 0 | 0 |
| AML42 | Depleted | 58 | 3 | 0 | 0 | 0 |
| AML43 | Depleted | 74 | 7 | 1 | 0 | NA |
| CTRL1 | Control | 11 | 0 | 0 | 0 | 0 |
| CTRL2 | Control | 3 | 0 | 0 | 0 | 0 |
| CTRL3 | Control | 8 | 0 | 0 | 0 | 0 |
| CTRL4 | Control | 88 | 5 | 0 | 0 | 0 |
| CTRL5 | Control | 62 | 5 | 0 | 0 | 0 |
| CTRL6 | Control | 29 | 5 | 0 | 0 | 0 |
| CTRL7 | Control | 63 | 0 | 0 | 0 | 0 |
| CTRL8 | Control | 19 | 0 | 0 | 0 | 0 |
| CTRL9 | Control | 46 | 1 | 0 | 0 | 0 |
| CTRL10 | Control | 34 | 3 | 0 | 0 | 0 |

AML: acute myeloid leukemia; CTRL: non-leukemic control; TLS: tertiary lymphoid structure; NA: the presence of TLS-like aggregates could not be assessed in these biopsies since a $CD20^+$ B cell stain was lacking.

**Supplementary Table 3.** Antibodies used for immunohistochemistry of bone biopsy tissue.

| Antibody | Code | Supplier | Catalog No. | Dilution |
|---|---|---|---|---|
| CD3 | 2GV6 | Roche | 05278422001 | NA |
| CD4 | SP35 | Roche | 05552737001 | NA |
| CD8 | SP57 | Roche | 5973248001 | NA |
| CD20 | L26 | Roche | 5267099001 | NA |
| CD15 | MMA | Roche | 5266904001 | NA |
| CD34 | QBEnd/10 | Roche | 6389320001 | NA |
| CD117 | EP10 | Roche | 790-7061 | NA |
| IgM | GA513 | Dako | GA51361-2 | 1:24.000 |
| IgG | GA512 | Dako | GA51261-2 | 1:60.000 |

NA: Not applicable.

# Figure 1

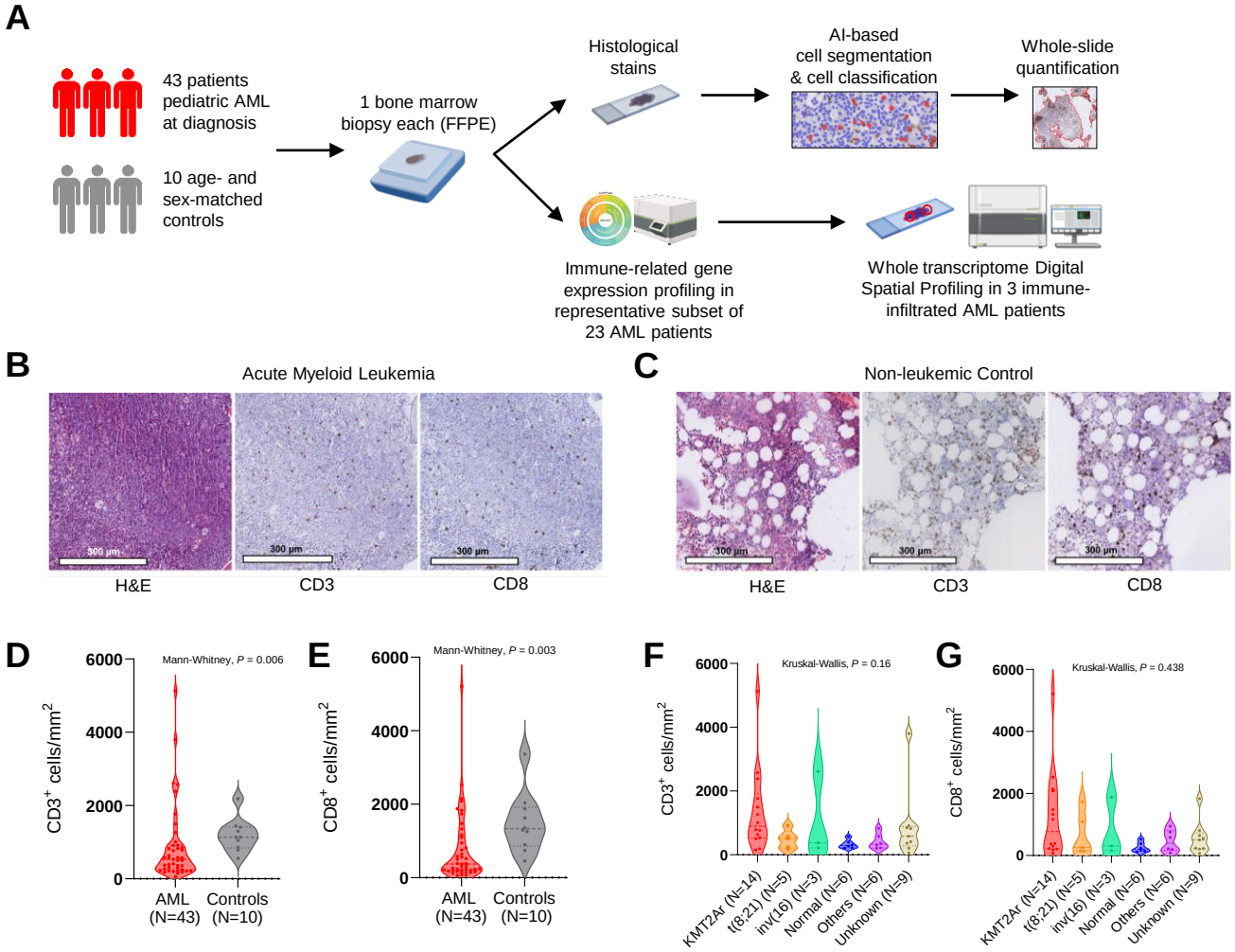
A
43 patients pediatric AML at diagnosis
10 age- and sex-matched controls
1 bone marrow biopsy each (FFPE)
Histological stains
AI-based cell segmentation & cell classification
Whole-slide quantification
Immune-related gene expression profiling in representative subset of 23 AML patients
Whole transcriptome Digital Spatial Profiling in 3 immune-infiltrated AML patients
B
Acute Myeloid Leukemia
H&E
CD3
CD8
C
Non-leukemic Control
H&E
CD3
CD8
300 µm
D
CD3+ cells/mm2
Mann-Whitney, P = 0.006
AML (N=43)
Controls (N=10)
E
CD8+ cells/mm2
Mann-Whitney, P = 0.003
AML (N=43)
Controls (N=10)
F
CD3+ cells/mm2
Kruskal-Wallis, P = 0.16
KMT2Ar (N=14)
t(8;21) (N=5)
inv(16) (N=3)
Normal (N=6)
Others (N=6)
Unknown (N=9)
G
CD8+ cells/mm2
Kruskal-Wallis, P = 0.438
KMT2Ar (N=14)
t(8;21) (N=5)
inv(16) (N=3)
Normal (N=6)
Others (N=6)
Unknown (N=9)

# Figure 2

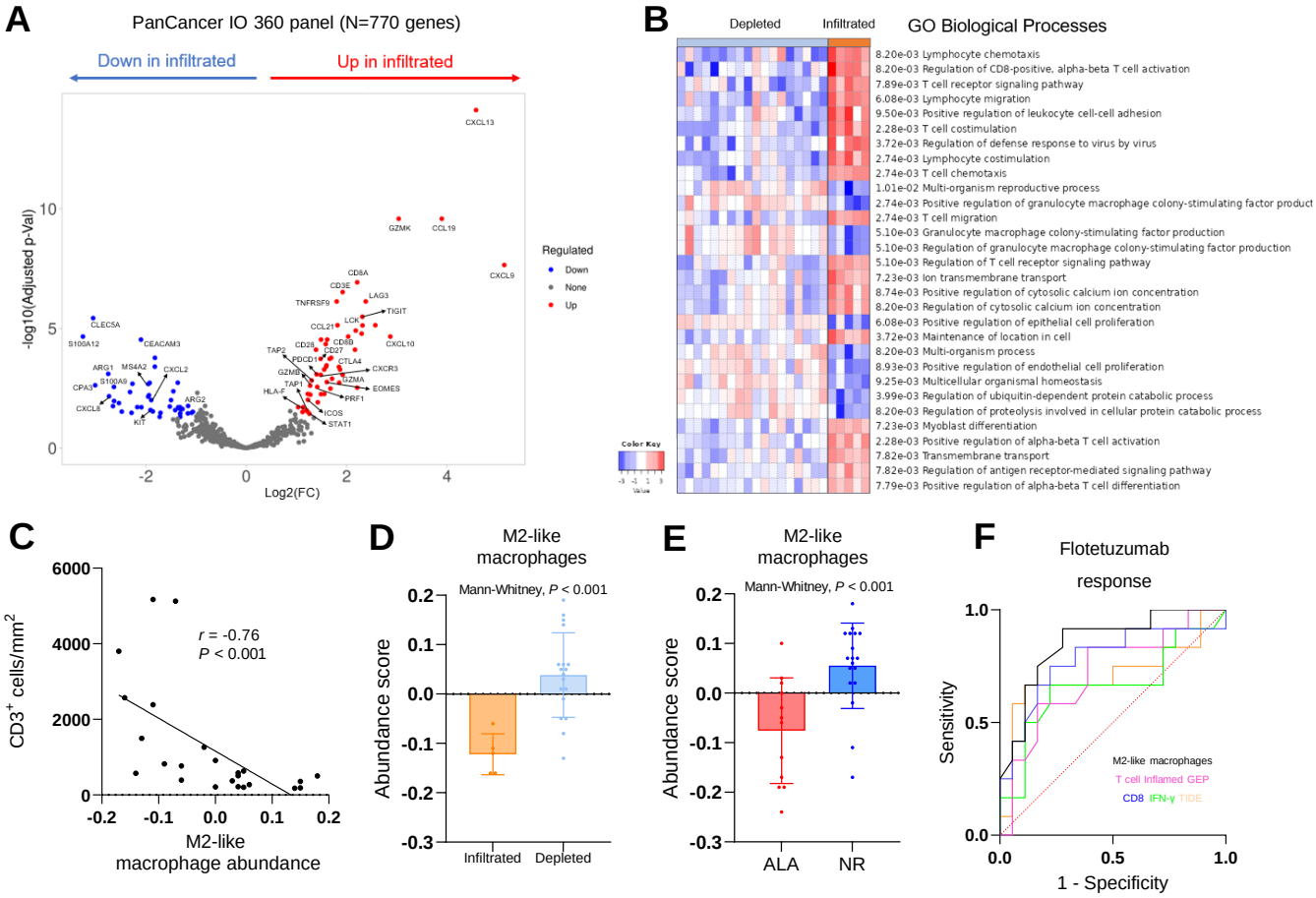
A
PanCancer IO 360 panel (N=770 genes)
Down in infiltrated
Up in infiltrated
-log10(Adjusted p-Val)
Log2(FC)
Regulated
Down
None
Up
B
Depleted
Infiltrated
GO Biological Processes
8.20e-03 Lymphocyte chemotaxis
8.20e-03 Regulation of CD8-positive, alpha-beta T cell activation
7.89e-03 T cell receptor signaling pathway
6.08e-03 Lymphocyte migration
9.50e-03 Positive regulation of leukocyte cell-cell adhesion
2.28e-03 T cell costimulation
3.72e-03 Regulation of defense response to virus by virus
2.74e-03 Lymphocyte costimulation
2.74e-03 T cell chemotaxis
1.01e-02 Multi-organism reproductive process
2.74e-03 Positive regulation of granulocyte macrophage colony-stimulating factor product
2.74e-03 T cell migration
5.10e-03 Granulocyte macrophage colony-stimulating factor production
5.10e-03 Regulation of granulocyte macrophage colony-stimulating factor production
5.10e-03 Regulation of T cell receptor signaling pathway
7.23e-03 Ion transmembrane transport
8.74e-03 Positive regulation of cytosolic calcium ion concentration
8.20e-03 Regulation of cytosolic calcium ion concentration
6.08e-03 Positive regulation of epithelial cell proliferation
3.72e-03 Maintenance of location in cell
8.20e-03 Multi-organism process
8.93e-03 Positive regulation of endothelial cell proliferation
9.25e-03 Multicellular organismal homeostasis
3.99e-03 Regulation of ubiquitin-dependent protein catabolic process
8.20e-03 Regulation of proteolysis involved in cellular protein catabolic process
7.23e-03 Myoblast differentiation
2.28e-03 Positive regulation of alpha-beta T cell activation
7.82e-03 Transmembrane transport
7.82e-03 Regulation of antigen receptor-mediated signaling pathway
7.79e-03 Positive regulation of alpha-beta T cell differentiation
Color Key
C
CD3+ cells/mm2
r = -0.76
P < 0.001
M2-like macrophage abundance
D
M2-like macrophages
Mann-Whitney, P < 0.001
Abundance score
Infiltrated
Depleted
E
M2-like macrophages
Mann-Whitney, P < 0.001
Abundance score
ALA
NR
F
Flotetuzumab response
Sensitivity
1 - Specificity
M2-like macrophages
T cell Inflamed GEP
CD8
IFN-γ
TIDE

# Figure 3

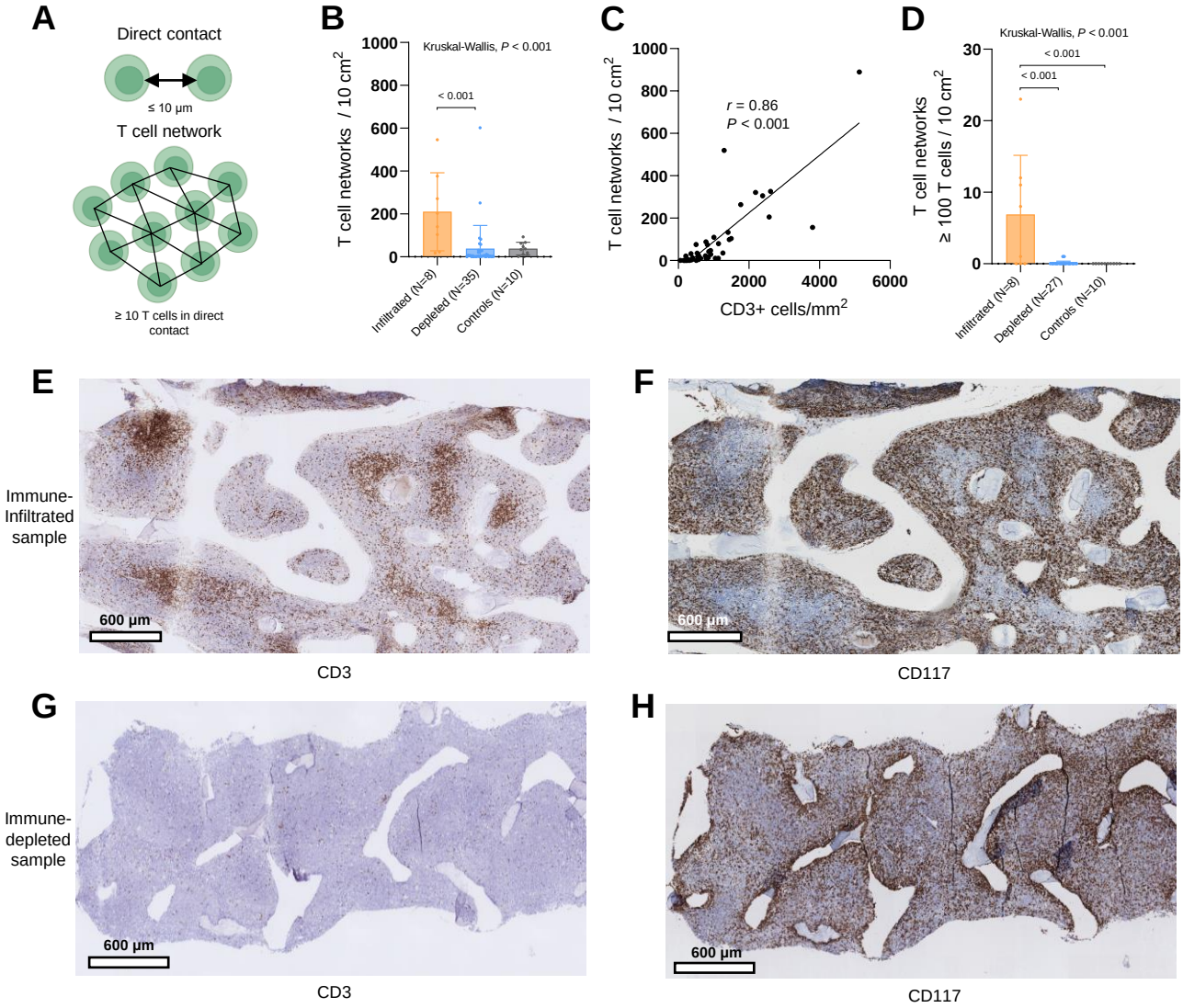
A
Direct contact
≤ 10 µm
T cell network
≥ 10 T cells in direct contact
B
Kruskal-Wallis, P < 0.001
< 0.001
T cell networks / 10 cm2
1000
800
600
400
200
0
Infiltrated (N=8)
Depleted (N=35)
Controls (N=10)
C
r = 0.86
P < 0.001
T cell networks / 10 cm2
CD3+ cells/mm2
0
2000
4000
6000
D
Kruskal-Wallis, P < 0.001
< 0.001
< 0.001
T cell networks ≥ 100 T cells / 10 cm2
30
20
10
0
Infiltrated (N=8)
Depleted (N=27)
Controls (N=10)
E
Immune-Infiltrated sample
600 µm
CD3
F
600 µm
CD117
G
Immune-depleted sample
600 µm
CD3
H
600 µm
CD117

# Figure 4

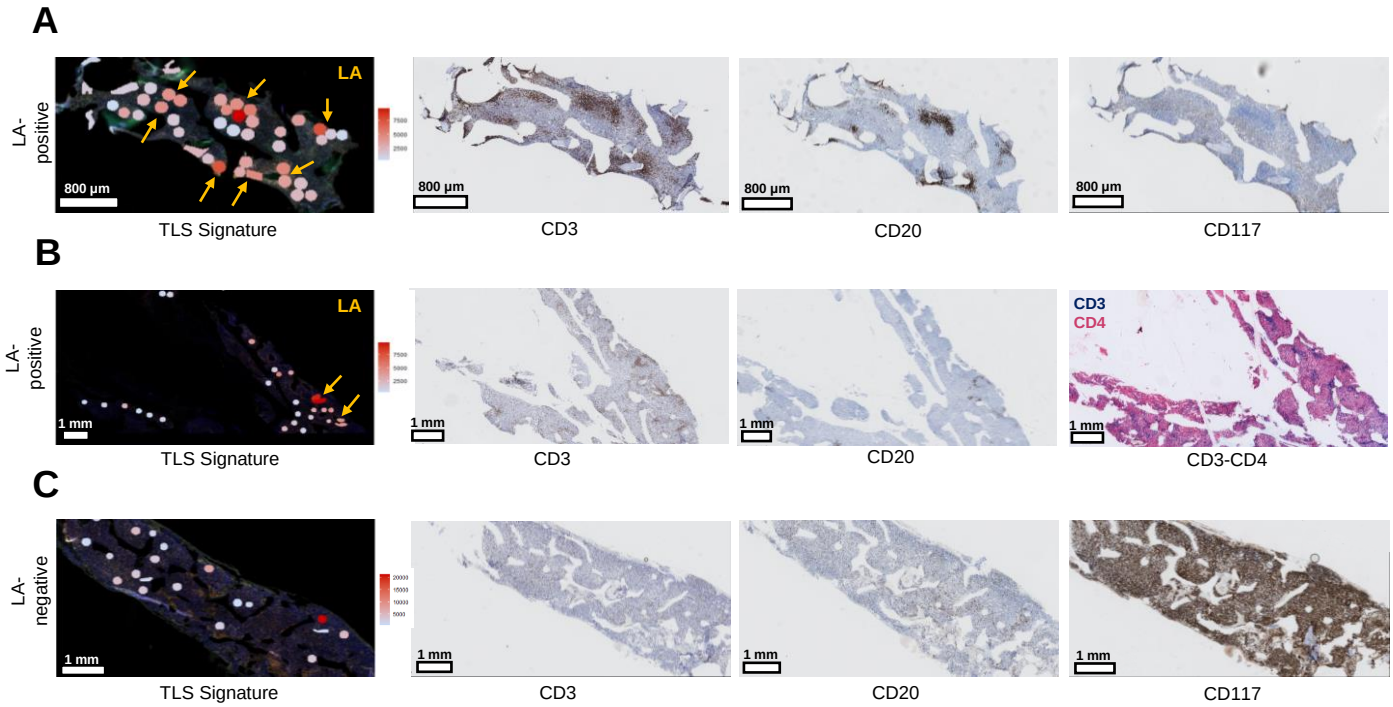
A
LA-positive
LA
800 µm
TLS Signature
CD3
CD20
CD117
B
LA-positive
LA
1 mm
TLS Signature
CD3
CD20
CD3
CD4
CD3-CD4
C
LA-negative
1 mm
TLS Signature
CD3
CD20
CD117

# Figure 5

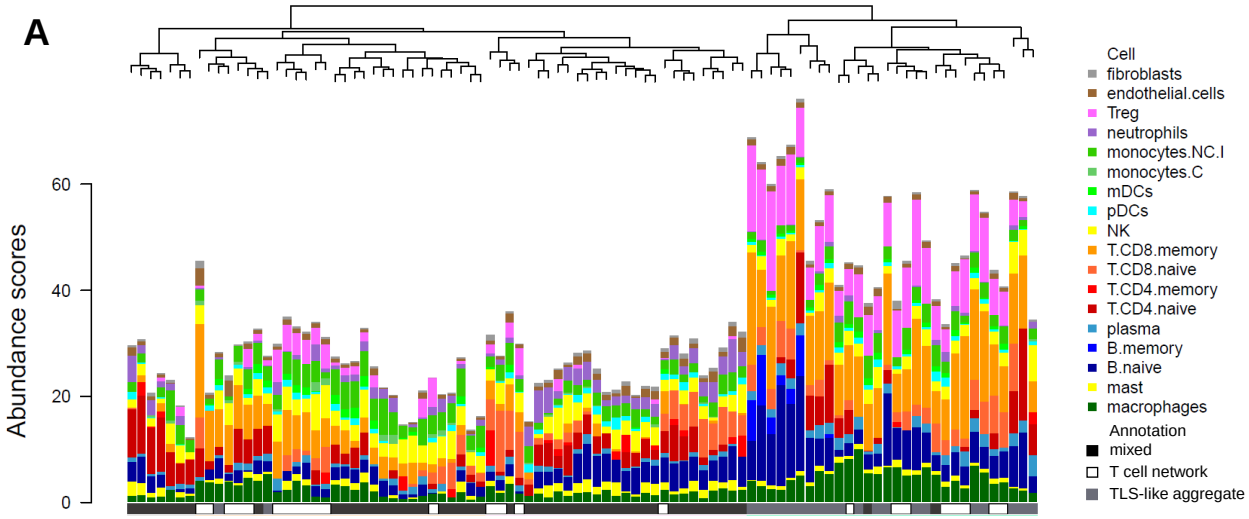
A
Abundance scores
60
40
20
0
Cell
fibroblasts
endothelial.cells
Treg
neutrophils
monocytes.NC.I
monocytes.C
mDCs
pDCs
NK
T.CD8.memory
T.CD8.naive
T.CD4.memory
T.CD4.naive
plasma
B.memory
B.naive
mast
macrophages
Annotation
mixed
T cell network
TLS-like aggregate

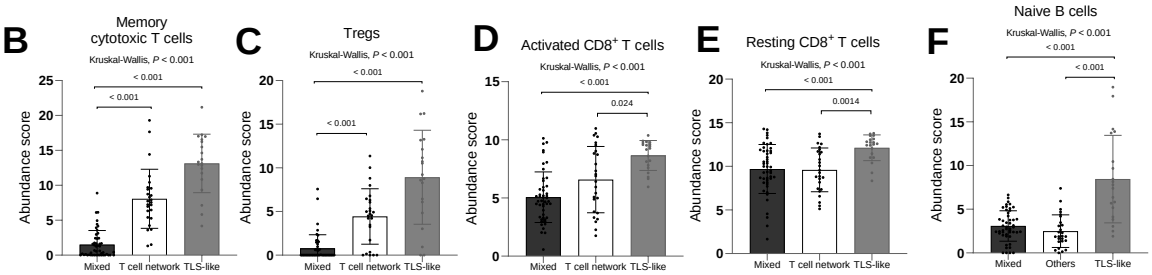
B
Memory cytotoxic T cells
Kruskal-Wallis, P < 0.001
< 0.001
< 0.001
Abundance score
Mixed
T cell network
TLS-like
C
Tregs
Kruskal-Wallis, P < 0.001
< 0.001
< 0.001
D
Activated CD8+ T cells
Kruskal-Wallis, P < 0.001
< 0.001
0.024
E
Resting CD8+ T cells
Kruskal-Wallis, P < 0.001
< 0.001
0.0014
F
Naive B cells
Kruskal-Wallis, P < 0.001
< 0.001
< 0.001
Mixed
Others
TLS-like

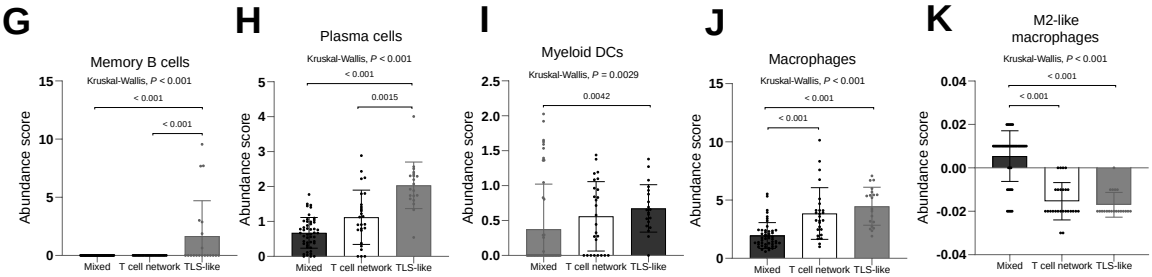
G
Memory B cells
Kruskal-Wallis, P < 0.001
< 0.001
< 0.001
H
Plasma cells
Kruskal-Wallis, P < 0.001
< 0.001
0.0015
I
Myeloid DCs
Kruskal-Wallis, P = 0.0029
0.0042
J
Macrophages
Kruskal-Wallis, P < 0.001
< 0.001
< 0.001
K
M2-like macrophages
Kruskal-Wallis, P < 0.001
< 0.001
< 0.001
Abundance score
Mixed
T cell network
TLS-like

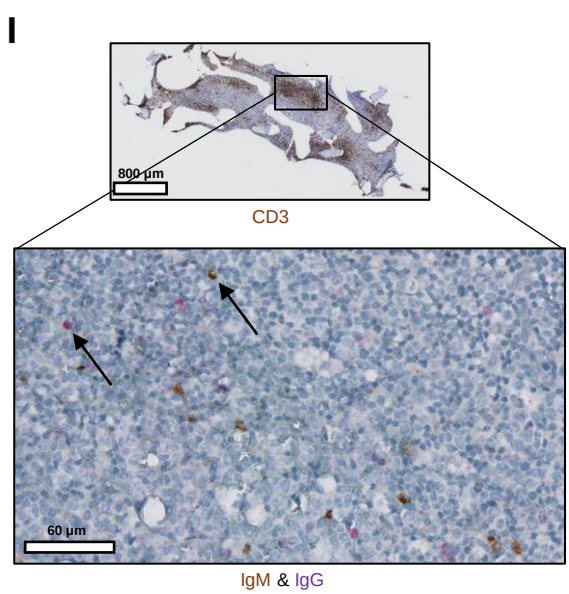
I
800 µm
CD3
60 µm
IgM & IgG

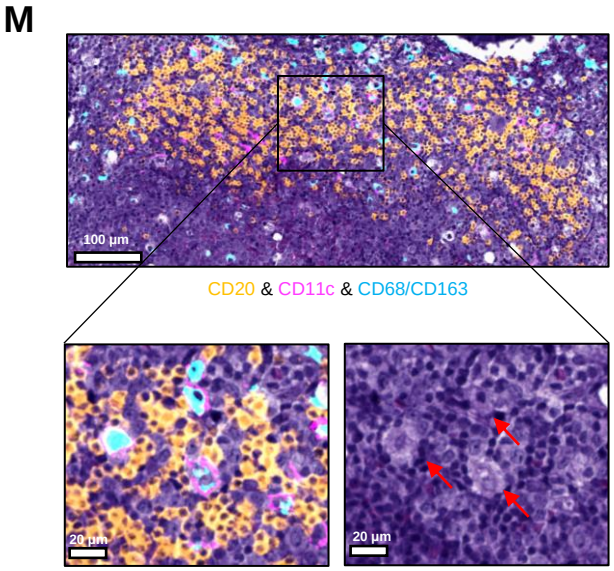
M
100 µm
CD20 & CD11c & CD68/CD163
20 µm
20 µm

# Figure S1

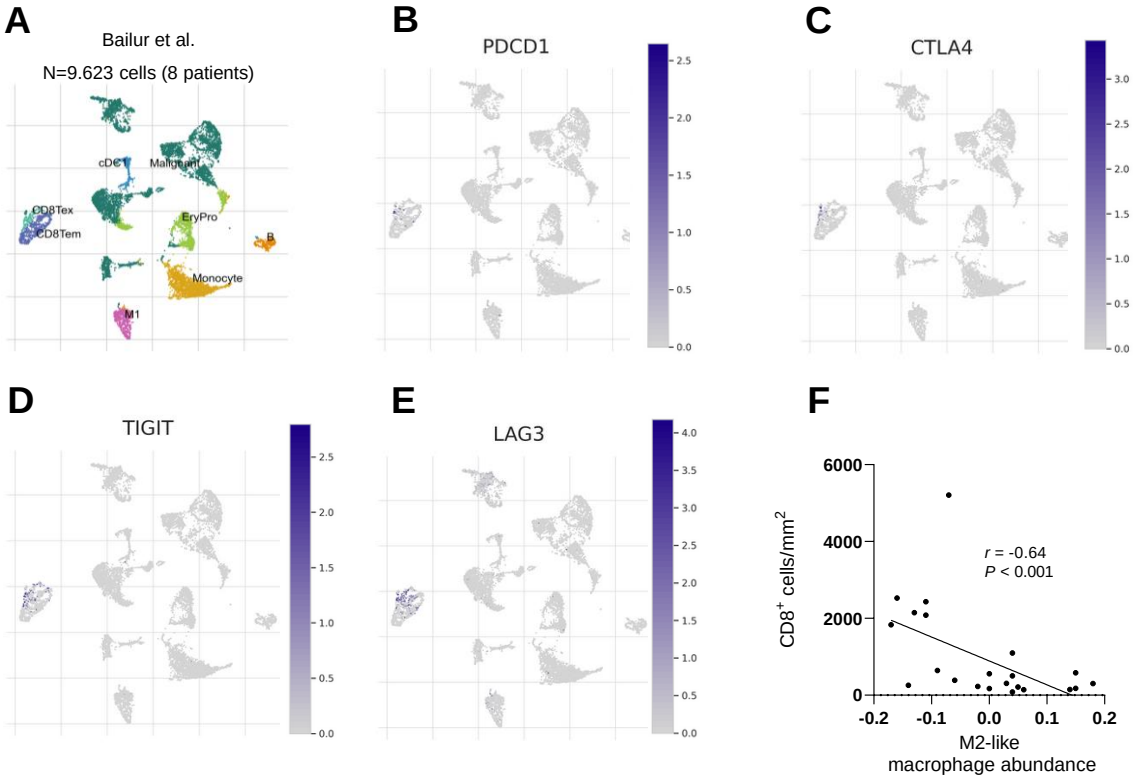
A
Bailur et al.
N=9.623 cells (8 patients)
cDC1
Malignant
CD8Tex
CD8Tem
EryPro
B
Monocyte
M1
B
PDCD1
C
CTLA4
D
TIGIT
E
LAG3
F
6000
4000
2000
0
-0.2
-0.1
0.0
0.1
0.2
r = -0.64
P < 0.001
CD8+ cells/mm2
M2-like
macrophage abundance

# Figure S2

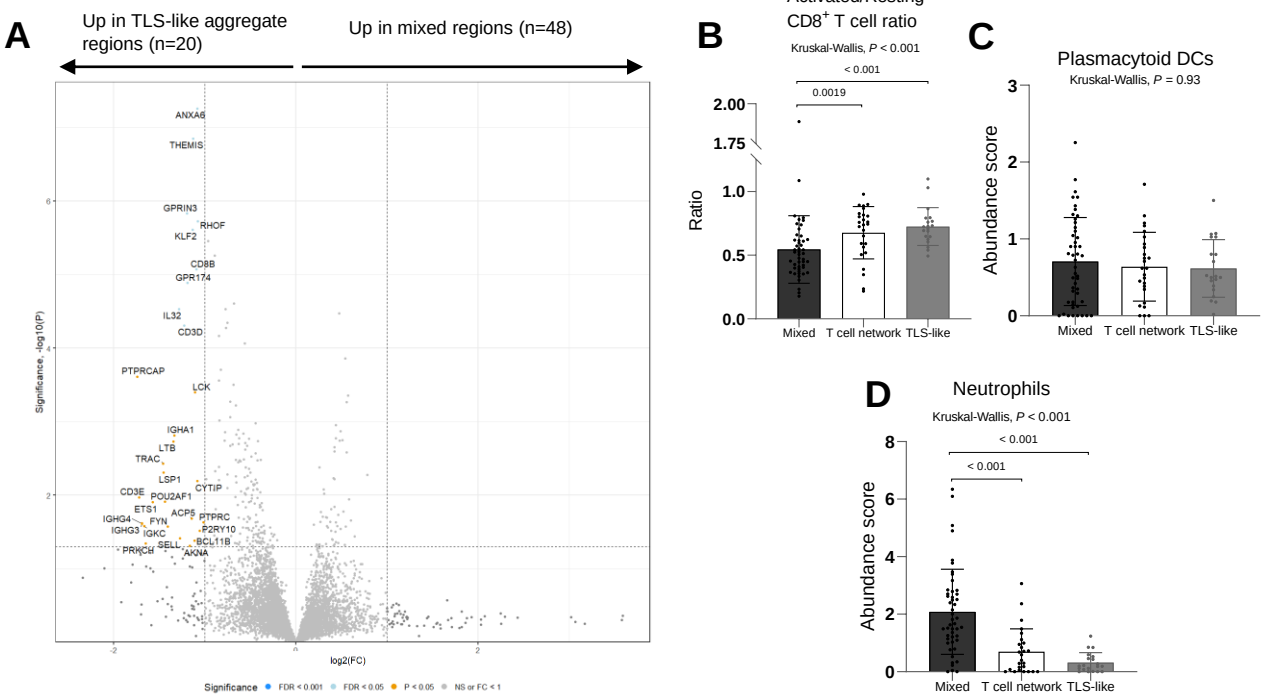
A
Up in TLS-like aggregate regions (n=20)
Up in mixed regions (n=48)
ANXA6
THEMIS
GPRIN3
RHOF
KLF2
CD8B
GPR174
IL32
CD3D
PTPRCAP
LCK
IGHA1
LTB
TRAC
LSP1
CYTIP
CD3E
POU2AF1
ETS1
ACP5
PTPRC
IGHG4
FYN
IGHG3
IGKC
P2RY10
BCL11B
PRKCH
SELL
AKNA
Significance, -log10(P)
log2(FC)
Significance
FDR < 0.001
FDR < 0.05
P < 0.05
NS or FC < 1
B
Activated/Resting CD8+ T cell ratio
Kruskal-Wallis, P < 0.001
< 0.001
0.0019
Ratio
Mixed
T cell network
TLS-like
C
Plasmacytoid DCs
Kruskal-Wallis, P = 0.93
Abundance score
Mixed
T cell network
TLS-like
D
Neutrophils
Kruskal-Wallis, P < 0.001
< 0.001
< 0.001
Abundance score
Mixed
T cell network
TLS-like

# Figure S3

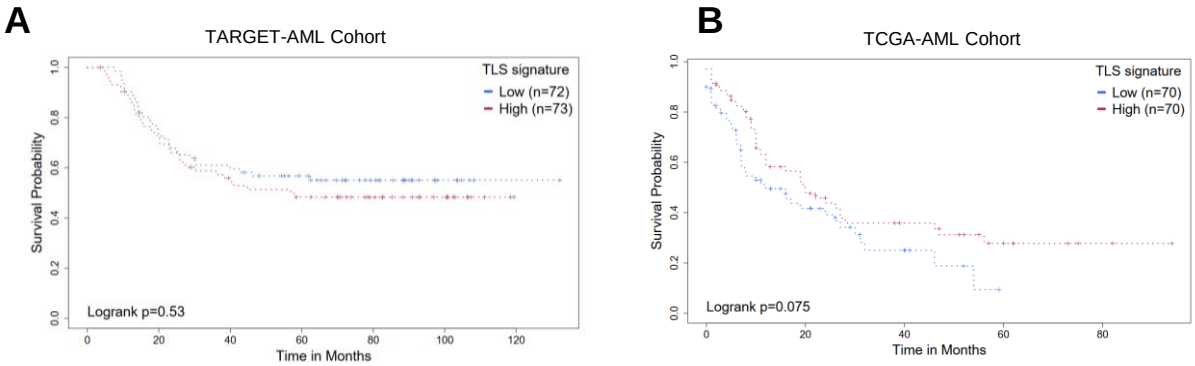
A
TARGET-AML Cohort
TLS signature
Low (n=72)
High (n=73)
Survival Probability
Logrank p=0.53
Time in Months
B
TCGA-AML Cohort
TLS signature
Low (n=70)
High (n=70)
Survival Probability
Logrank p=0.075
Time in Months